Role of niobium and oxygen concentration on glass forming ability and crystallization behavior of Zr-Ni-Al-Cu-Nb bulk metallic glasses with low copper concentration

K.M. Cole [a,*], D.W. Kirk [b], C.V. Singh [a], S.J. Thorpe [a]

[a] Department of Materials Science and Engineering, University of Toronto, 184 College St., Toronto, Ontario M5S3E4, Canada
[b] Department of Chemical Engineering and Applied Chemistry, University of Toronto, 200 College St., Toronto, Ontario M5S3E4, Canada

ABSTRACT

Arc melting and suction casting was used to prepare $(Zr_{57}Ni_{20}Al_{15}Cu_8)_{100-x}Nb_x$ bulk metallic glass alloys with Nb concentration ranging from 1.9 to 4.3 at.%. The glass forming ability and crystallization behavior of these alloys were investigated using X-ray diffraction (XRD), scanning electron microscopy (SEM), and differential scanning calorimetry (DSC). By varying the Nb concentration, a high glass forming range between 2 and 4 at.% Nb was observed in XRD and SEM. It was also revealed that oxygen has a detrimental effect on the GFA within this high glass forming range and the severity was closely linked to the state in which oxygen was present. Since thermal activation is an intrinsic property of crystallization, the activation energy for crystallization was computed from Kissinger, Ozawa and Cheng's methods based on non-isothermal DSC data. A comparison of activation energy models revealed that Kissinger and Ozawa show similar trends while Cheng's method depicted varied results for samples containing pre-existing crystals. For amorphous samples, Kissinger and Ozawa showed the highest value of activation energy (316 kJ/mol and 329 kJ/mol, respectively) at 2.7 at.% Nb, which is consistent with the supercooled liquid region and resulting in higher glass forming ability at this composition.

© 2016 Elsevier B.V. All rights reserved.

1. Introduction

Bulk metallic glasses (BMGs) possess a unique combination of mechanical and chemical properties due to the absence of crystalline features [1–3]. Since their emergence, a large number of alloys have been cast with high glass forming ability (GFA) and thermal stability [4–6]. The crystallization behavior and GFA of BMGs are very sensitive to alloy composition [7–9]. Minor alloying additions can have a variety of effects on both material properties and crystallization behavior, but are most commonly used as an effective method for improving the GFA of a system and aid in suppressing crystallization [6]. Specifically, minor alloying additions can improve GFA due to an increase in the supercooled liquid region, which helps to retard crystallization [2,6,10]. Even small variations in the concentration of minor alloying element additions can result in differing crystallization pathways and associated kinetics, significantly affecting the phase stability and GFA [11].

For instance, the $Zr_{65-x}Ni_{10}Al_{10}Cu_{15}Nb_x$ alloy has been shown to achieve the largest casting thickness for 2.5 at.% Nb [9], yet for a very similar $Zr_{62-x}Ni_{12.6}Al_{10}Cu_{15.4}Nb_x$ alloy, Dong et al. [12] have shown that the optimal Nb concentration is 5 at.% Nb. The optimum Nb concentration for obtaining highest GFA (or critical casting diameter as a result) is heavily dependent on the position of a deep eutectic point in the phase space since eutectic liquids are energetically more stable [13]. Thermal stability of the supercooled liquid region is therefore an effective way to characterize and rank BMG compositions. Since the crystallization behavior of BMGs is directly related to material properties, it is important to understand the role of minor alloying elements for each alloy composition in order to utilize these properties to create amorphous structures or control mechanical and chemical properties. For example, BMG composites can be formed by inducing partial crystallization either upon casting or annealing in order to increase the ductility of the material [7,14,15,16,17]. Similar effects on crystallization behavior can be seen as a result of impurities such as oxygen. Zirconium based BMGs are especially sensitive to oxygen, which often causes metastable quasi-crystalline structure to form upon casting [6,18–20].

Recently, a new $Zr_{56}Ni_{20}Al_{15}Cu_5Nb_4$ alloy with a diameter up to 25 mm was cast through copper mold casting by Li et al. [21]. This alloy possessed a high yield strength of 1915 MPa, a large plastic strain of 5.5%, a Young's modulus of 100 GPa and displayed excellent corrosion resistance in sulfuric acid (H_2SO_4) and chloride-ion-containing solutions [21]. Comparing these mechanical properties with the conventional $Zr_{57}Ni_{12.6}Al_{10}Cu_{15.4}Nb_5$, it can be seen that this new composition resulted in an increased yield strength (1915 vs. 1800 MPa) and the Young's

* Corresponding author.
 E-mail address: kevin.cole@mail.utoronto.ca (K.M. Cole).

modulus (100 vs. 86.7 GPa) [22]. Furthermore, it should be noted that the typical Zr-based BMGs with high Cu content (12.5–36 at.%) are susceptible to corrosion in H_2SO_4 and chloride-ion-containing environments. Reduction in the Cu concentration in this alloy improved its corrosion resistance deeming it a promising material when combined with the attributes of a high casting diameter and good mechanical properties [21,23,24]. To further assess the benefits of this alloy, the thermal stability and crystallization behavior need to be examined.

Although the effect of Nb concentration on crystallization behavior and GFA in BMGs with high Cu content has been previously studied [9,11], the conclusions drawn in these studies cannot be directly translated to crystallization mechanisms in alloys with low Cu content due to significant changes in major element concentrations. It is hence important to understand the effects of Nb concentration on the thermal stability and GFA of these alloys to optimize their composition and increase their critical casting diameter. In this work, the authors have studied the effects of Nb concentration on the crystallization behavior within low Cu content Zr-Ni-Al-Cu-Nb alloys cast through arc melting and suction casting into a copper mold. The crystallization behavior was analyzed using XRD and DSC, with further investigation through scanning electron microscopy (SEM). Activation energy was calculated and compared from DSC data using Kissinger, Ozawa and Cheng's method to study crystallization behavior and GFA.

2. Experimental

Ingots with nominal compositions of $(Zr_{57}Ni_{20}Al_{15}Cu_8)_{100-x}Nb_x$ were prepared through arc melting and suction casting into a copper mold. The metals, in the form of slugs, Zr – high purity (99.95 wt.% with 580 ppm O_2), Zr – low purity (99.5 wt.% with 1400 ppm O_2), Ni (99.98 wt.%), Al (99.999 wt.%), Cu (99.995 wt.%) and Nb (99.95 wt.%) were weighed using a Mettler AE260 balance before being placed in the arc melter (Edmund Büher Compact Arc Melter MAM-1). Before melting, the caster was vacuumed down to approximately 0.1 mbar using a roughing pump and then filled back to atmosphere pressure using high purity argon (99.9999%). This step was repeated five times for each sample to ensure the oxygen content remained consistent. Each ingot was then melted four times for 15 s under the high purity argon. Between each melting step, the ingot was flipped to achieve improved chemical homogeneity before being finally suction cast after the fourth melting cycle. For one of the samples (Sample II), the casting technique was varied to a cast-recast method to analyze the effect of pre-existing oxide on crystallization behavior. The cast-recast method involved taking a cast rod, cutting it into several small pieces, and placing it back into the arc melter to be remelted for 15 s before being cast again.

Rod samples were prepared with a diameter of 3 mm and length of 30 mm, and were sectioned using a diamond blade cutter for testing. This diameter was chosen for investigation such that it would comply with all required testing equipment. Samples were progressively ground on 400, 600, and 1200 grit SiC paper before being polished to a final surface finish of 1 μm using diamond paste. X-ray diffraction with Cu K_α was used to analyze the structure of the rods from 20 to 80° at a scan speed of 6 s per 0.03° step size (Rigaku Miniflex 600). The rods were imaged and inspected for crystals using high resolution SEM (Hitachi SU3500). Energy-dispersive X-ray spectroscopy (EDX) was used at 20 kV during SEM to determine as-cast compositions.

Inert gas fusion was conducted to determine the oxygen content in the as-cast rods (LECO ON736). As per industry standard, preparation and testing was conducted according to ASTM E1409-13 [25]. To ensure reproducibility, rods were sectioned into 0.14 g samples using a diamond blade before testing. Before each test, zirconium samples with known oxygen values were used to calibrate the equipment and provide accurate readings of oxygen content. Through calibration, an error of ± 0.01 wt.% oxygen was obtained.

The glass transition (T_g), and crystallization (T_x) temperatures of the rods were determined through DSC (TA Instruments Q20) using heating rates (β) of 2.5 K/min, 5 K/min, 10 K/min, 20 K/min and 40 K/min under a high purity argon flow. Enthalpy of crystallization and activation energy (E_a) was measured with DSC as well. Each sample was prepared using 15–20 mg and referenced against an empty hermetic aluminum pan.

3. Results and discussion

Table 1 lists several as-cast $(Zr_{57}Ni_{20}Al_{15}Cu_8)_{100-x}Nb_x$ (from x = 1.9 to 4.3 at.%) alloy rods with a diameter of 3 mm made through arch melting and suction casting into a copper mold. Relevant casting parameters and the resulting microstructure caused by variation in Nb and oxygen concentration as a result of cast-recast method or lower purity Zr are also tabulated. In this study, an input composition of $Zr_{57}Ni_{20}Al_{15}Cu_{8-x}Nb_x$ was used. The compositions listed in Table 1 are the as cast compositions that were measured using EDX. Slight variations in elemental content are a result of crystallization pathways and fabrication methods using EDX as a means of estimating compositional variations of ± 0.5 at.% that can be expected.

3.1. Effect of Nb

Fig. 1 shows the XRD patterns for all the samples listed in Table 1. It can be seen that the crystallization behavior changes with increase in either Nb or oxygen concentration. XRD revealed that for the alloy containing less than 2 at.% Nb (Sample I), the GFA is not sufficient enough to suppress the formation of $Zr_3NiO_{1.17}$ and $CuZr_2$ crystals. As the Nb content was increased to 2.7 at.% (Sample III), an amorphous structure is produced, as noted by the complete lack of crystalline peaks in the XRD spectra and no observation of crystals in the corresponding SEM image (Fig. 2, III). The amorphous structure continued to be formed up to 4 at.% Nb (Sample V). It should be noted that even though both XRD and SEM results show these samples to be amorphous; very small and low volume fractions of phases beyond the detection limit of XRD and resolution of SEM cannot be ruled out. Once the Nb content is above 4 at.% (Sample VI), the beneficial effect of Nb addition on GFA was lost and once again $Zr_3NiO_{1.17}$ and $CuZr_2$ crystals were observed, along with $Nb_{0.94}O_{0.06}$ crystals due to the increased Nb concentration. These results suggest the possibility that there is a deep eutectic point between 2 and 4 at.% Nb that helps to stabilize the liquid and preventing crystallization from occurring, thereby creating an ideal casting range for this low Cu alloy system [13]. This ideal casting range is consistent with results seen for similar alloys by Inoue et al. [9] and Li et al. [21]. Fig. 3 depicts possible crystallization pathways as a function of Nb concentration within the alloy. These results have been further confirmed by SEM imaging and show the formation of crystals noted above (Figs. 2 and 3).

3.2. Effect of oxygen

Even if the alloy contains a favorable amount of Nb (2–4 at.%), the presence of oxygen has been reported to hinder its GFA. It is well known that excess oxygen is harmful to the GFA of many BMG systems; however, the state in which oxygen exists can also have a great effect on

Table 1
Casting conditions used to suction cast 3 mm diameter rods of Zr-Ni-Al-Cu-Nb alloys.

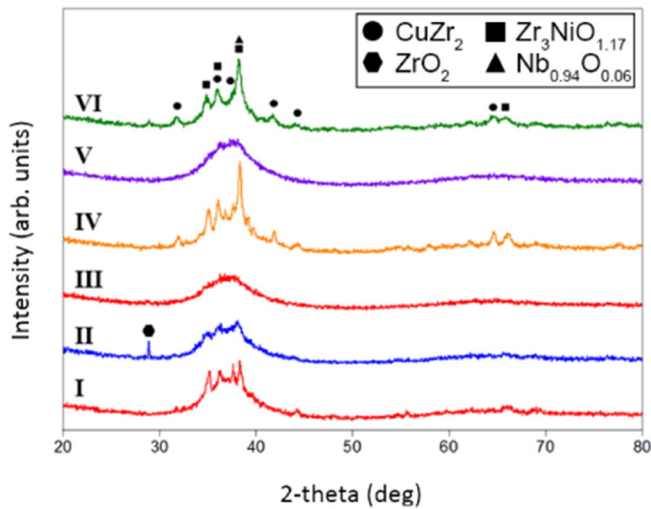| Sample	EDX comp. (at.% ± 0.5%)	Zr purity	Casting	Observation
I	$Zr_{58.8}Ni_{20.0}Al_{14.5}Cu_{4.8}Nb_{1.9}$	High	Suction	Partially crystalline
II	$Zr_{55.4}Ni_{21.3}Al_{15.4}Cu_{5.4}Nb_{2.5}$	High	Cast-recast	Partially crystalline
III	$Zr_{55.5}Ni_{20.6}Al_{14.7}Cu_{6.5}Nb_{2.7}$	High	Suction	Amorphous
IV	$Zr_{55.0}Ni_{20.3}Al_{15.9}Cu_{5.3}Nb_{3.6}$	Low	Suction	Partially crystalline
V	$Zr_{54.9}Ni_{19.9}Al_{15.0}Cu_{6.3}Nb_{3.9}$	High	Suction	Amorphous
VI	$Zr_{54.5}Ni_{20.7}Al_{15.2}Cu_{5.2}Nb_{4.3}$	High	Suction	Partially crystalline

Fig. 1. XRD patterns taken for all as-cast samples (Compositions for I–VI given in Table 1).

the GFA [18-20,26]. Since oxygen exists as either a solute element or part of an oxide, it can result in varying crystallization pathways upon casting. The severity of oxygen as either a solute element or oxide on GFA is important to understanding the processing of BMGs and obtain an amorphous structure.

The influence of oxygen on the crystallization mechanisms of the alloy was studied by individually examining its effect when it is present as a solute element and as an oxide. The concentration of oxygen as a solute was varied by changing the oxygen content of the input materials. High purity Zr (99.95 wt.% with 580 ppm O_2, and low purity Zr (99.5 wt.% with 1400 ppm O_2) was used to produce samples with varying oxygen solute concentrations. Two samples (IV and V) of a similar compositions were cast using Zr with high and low concentrations of oxygen. The output of the gas fusion measurements is summarized in Table 2 below. Oxygen content measurements confirmed that the use of low purity Zr resulted in a two fold increase in the oxygen present in the alloy. The higher oxygen concentration in Sample IV resulted in crystallization of the supercooled liquid and the formation metastable phases as seen in Figs. 1IV and 2IV. The presence of these metastable crystals was also confirmed by DSC (Fig. 4, sample IV). The absence of multiple crystallization peaks could be attributed to pre-existing phases formed during casting. Ultimately, the presence of metastable phases destabilizes the supercooled liquid, reducing the GFA of the alloy [6]. The above findings are consistent with observations reported for similar alloy compositions [18,19,20].

To study the effects of a pre-existing oxide, two samples of a similar composition (Samples II and III) were cast using the high purity Zr. Sample II was prepared using the cast-recast method to introduce oxygen in the form of a solid oxide layer. Once cast, the sample was examined by XRD to ensure the presence of the oxide phase in the alloy, see Fig. 1. The sharp peak (29°) found in the spectra is attributed
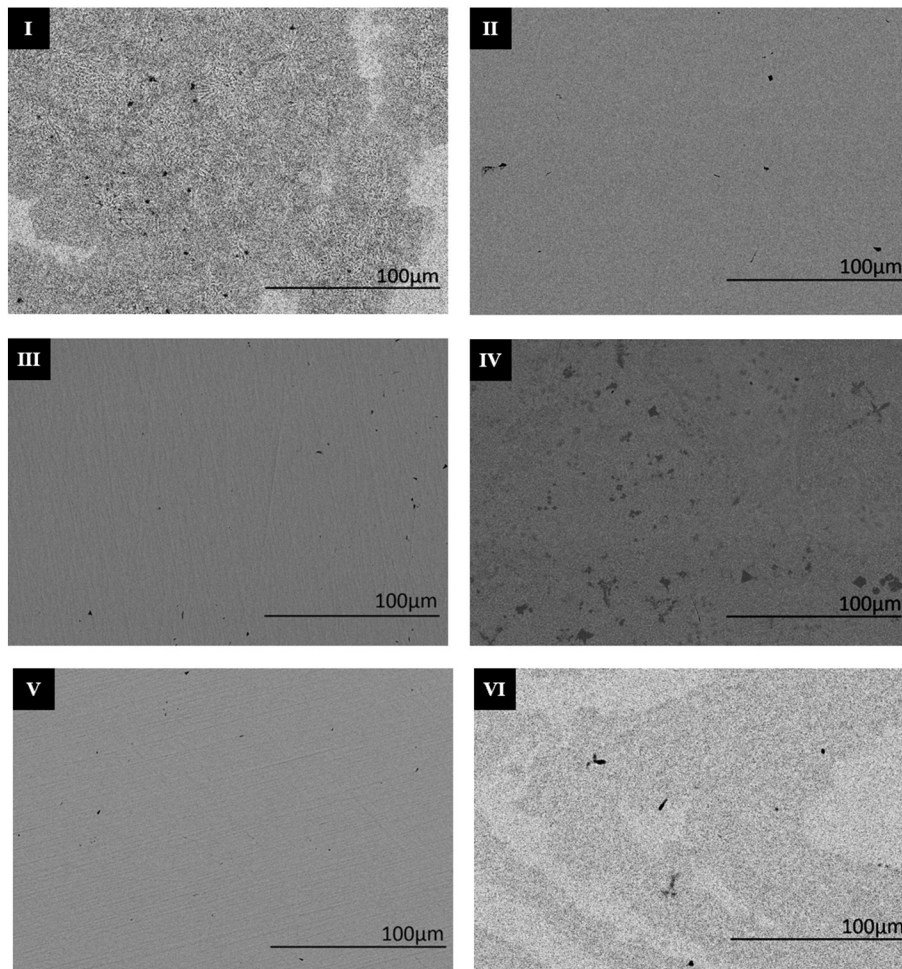

Fig. 2. SEM micrographs for cross-sections for as-cast rods taken at 500× magnification to compare crystalline features. Samples I, IV and VI show clear dendritic crystal formation. Samples II, III and V do not show any indication of crystals; however, XRD indicates oxides are present in Sample II that cannot be seen in SEM.
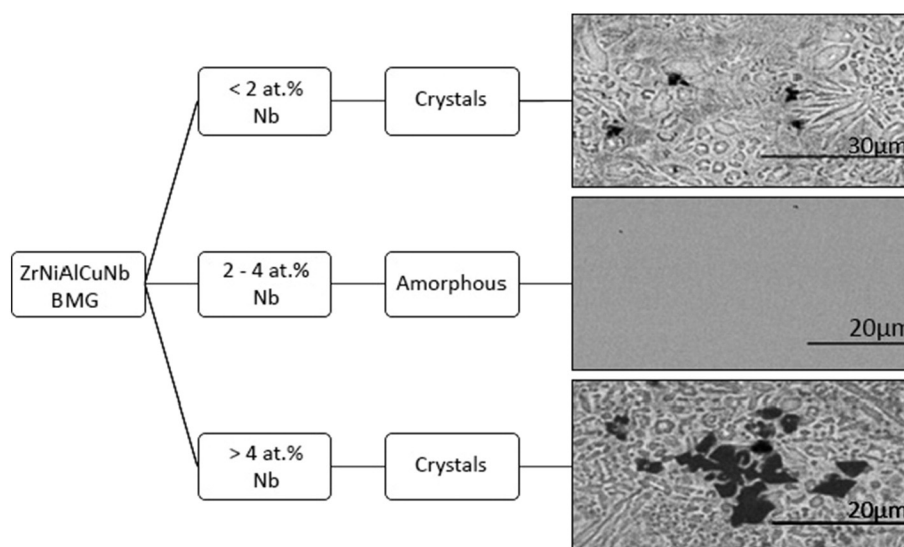
Fig. 3. Effect of Nb concentration on the crystallization behavior noted in XRD, showing a high GFA range from 2 to 4 at.% Nb.

to the oxide layer (ZrO_2) that was formed during the first cast. During the re-cast the oxide present on the surface of the sample was introduced into the alloy. It is worth noting that even though this oxide can clearly be seen in XRD, there is only slight signs of metastable crystal formation compared to the sample prepared with low purity Zr (Sample IV). No observation of crystals or oxides was seen during SEM (Fig. 2, sample II), further indicating that crystallization was minimal. The output of this investigation suggests that the influence of oxygen on the crystallization behavior of the alloy is closely related to the form in which it is present. When oxygen is present in a solute form it destabilizes the supercooled liquid region due to the formation of metastable crystals, while its presence as an oxide is relatively less harmful to forming an amorphous alloy. Similar observations were reported previously [18,19,26].

It should be noted that the role of oxygen in BMG synthesis is more complex than appears from the findings of this investigation. While the current findings suggest that the presence of oxygen in solute or oxide form reduces the GFA of the alloy, other investigations found that oxygen levels below a certain threshold can promote crystallization [20,26]. These studies have shown that reducing oxygen below a certain level can cause crystallization to occur and that a certain amount of oxygen is needed to produce an amorphous structure. In the current investigation, Sample I shows a high degree of crystallinity even though it has the lowest oxygen content. Consequently, it can be concluded that reduction of oxygen content in the alloy is not always the preferred strategy to increase its GFA. In this case minor alloying (Nb above 2 at.%) can be seen to be a more effective approach to stabilize the supercooled liquid region promoting the formation of BMGs.

3.3. Thermal stability and kinetics

To investigate the crystallization kinetics of these alloys, DSC scans were conducted at varying heating rates ranging between 2.5 and 40 K/min. Fig. 4 shows a comparison between DSC curves for all samples listed in Table 1, measured at a heating rate of 10 K/min. Amorphous alloys (III and V) show a glass transition followed by multi-step exothermic crystallization peaks, while as-cast partially crystalline samples (I, II,

IV and VI) show a single exothermic crystallization peak. Amorphous samples follow a multi-step crystallization mechanism beginning with the formation of cubic Zr_2Ni (c-Zr_2Ni) that will transform into tetragonal Zr_2Ni (t-Zr_2Ni) and Zr_5Ni_4Al [27,28]. Each crystallization step is represented by a separate peak on the DSC curve (as seen in Fig. 5). Further characterization of the GFA and degree of crystallinity of the alloy can be done by estimating its enthalpy of crystallization (ΔH). Typically, partially crystalline samples exhibit lower values of ΔH, as the crystallites present in their microstructure act as nucleation sites that lower the activation energy required for crystallization. Amorphous samples exhibit higher values of ΔH due to the limited number of nucleation sites and greater thermal stability. Previously reported research clearly indicated that alloy systems with a large supercooled liquid region, had greater enthalpy of crystallization and better glass forming ability [29]. In this investigation the enthalpy of crystallization for each sample was estimated from the area under the crystallization peaks. It was found that amorphous samples showed an average ΔH of 82 J/g while the average ΔH for partially crystalline samples was 68 J/g, both being greater than the enthalpy calculated for the $Zr_{55}Cu_{30}Al_{10}Ni_5$ alloy by Lin et al. [28].

A deeper insight into the crystallization kinetics of the amorphous samples can be gained by examining the enthalpy associated with
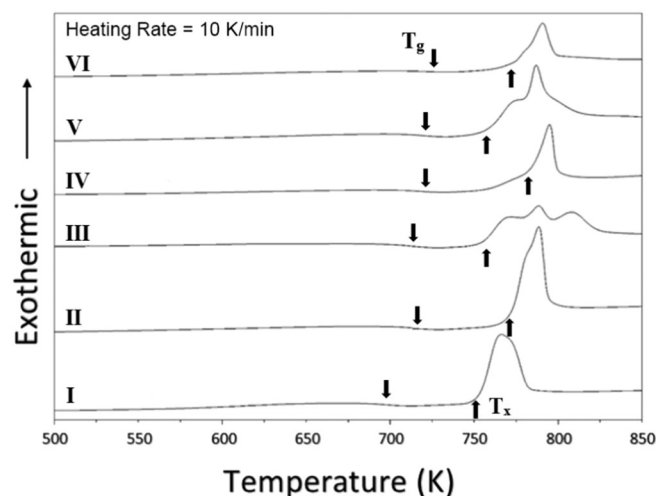

Fig. 4. DSC comparison for all as-cast samples at a heating rate of 10 K/min.

Table 2
Oxygen content (wt.%) for each sample measured using inert gas fusion.

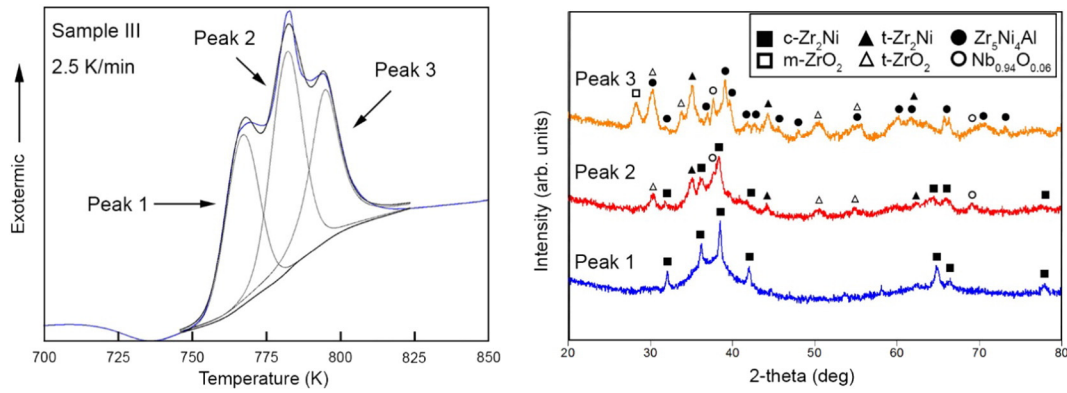| Sample	I	II	III	IV	V	VI
Oxygen (wt.% ± 0.01)	0.06	0.08	0.08	0.13	0.07	0.11

Fig. 5. Deconvoluted crystallization peaks for Sample III at a heating rate of 2.5 K/min with corresponding XRD scans to identify existing phases at each peak step.

each crystallization step. Since every phase transformation is associated with a separate peak on the DSC curve, it is possible to estimate its individual enthalpy of crystallization by measuring the area of the fitted peak. The individual enthalpy of crystallization can then provide insight into the crystallization pathway, and its overall contribution to the enthalpy of the crystallization process. Fig. 5 demonstrates an example of the fitting procedure used to deconvolute the DSC curves and separate out the contribution from each crystallization step. It was observed that as the heating rate was increased from 2.5 to 40 K/min, the first peak, corresponding to the formation of c-Zr_2Ni crystals, only gradually increased while the second peak (t-Zr_2Ni) decreased and the third peak (Zr_5Ni_4Al) increased much more than the first one. The growth of the first DSC peak in response to increased heating rate, signified the importance of this step to the overall crystallization mechanism. It can be concluded that c-Zr_2Ni is required as a precursor before any further phase transformation can occur. The above can be further confirmed by examining the XRD spectra given in Fig. 5, showing a sequential reduction in the presence of c-Zr_2Ni as the sample was heated from peaks 1 to 3. The observed reduction in the magnitude of the second peak on the DSC curve in response to increased heating rates indicates there are two crystallization pathways. As the heating rate increased, the crystallization pathway favors the formation of Zr_5Ni_4Al and will bypass the t-Zr_2Ni phase.

The present section examined the crystallization mechanisms of amorphous $Zr_{57}Ni_{20}Al_{15}Cu_8)_{100-x}Nb_x$ alloys by coupling DSC and XRD techniques. Deconvolution of individual DSC peaks provided insight into the role and stability of each intermediate phase, while XRD provided important information on the chemistry and structure of these phases. Analysis of sequential XRD measurements at each crystallization peak elucidated the phase transformations occurring during crystallization.

Other thermal properties such as glass transition temperature (T_g), crystallization temperature (T_x), supercooled liquid region ($\Delta T_x = T_x - T_g$), and initial activation energies have been determined from the DSC curves seen in Fig. 4. Table 3 shows the T_g, T_x, and ΔT_x for amorphous samples (III and V). These thermal properties are known to be important correlating factors that influence the GFA and crystallization behavior of these alloys. In particular, a large supercooled liquid region and large activation energy would indicate that the material

has good thermal stability and increases the ability to retard crystallization [10]. These results, along with activation energies, are further discussed below.

The activation energies were determined using three different non-isothermal equations; Kissinger, Ozawa and Cheng [30,31,32]. Both the Kissinger and Ozawa equations assume first order reactions that do not factor in the concept of nucleation and growth [33]. They most commonly use the peak temperature from first crystallization event in DSC to derive the activation energy [32,33]. Cheng's equation follows similar criteria but uses the temperature from the first inflection point whereby the crystallization rate is at a maximum [32]. Beginning with the Kissinger equation, we have [30]:

$$\ln \frac{T_p^2}{\beta} = \frac{E_a}{RT} + \ln \frac{E_a}{R} - \ln \nu \qquad (1)$$

where T_p is the peak temperature of the first crystallization peak, β is the heating rate, E_a is the activation energy, ν is the frequency factor, and R denotes the gas constant. The activation energy is then taken to be the product of the gas constant and the slope of the linear fitting line when plotting $\ln (T_p^2/\beta)$ versus 1000/T, as seen in Fig. 6. Alloys having a shallow slope, i.e. with a high activation energy, will have greater thermal stability. Error range was determined by performing tests over multiple samples at the same heating rate, as noted in the top right corner of Fig. 6. Importantly, this range of error was noted to be within the error of the equipment, indicating good reproducibility
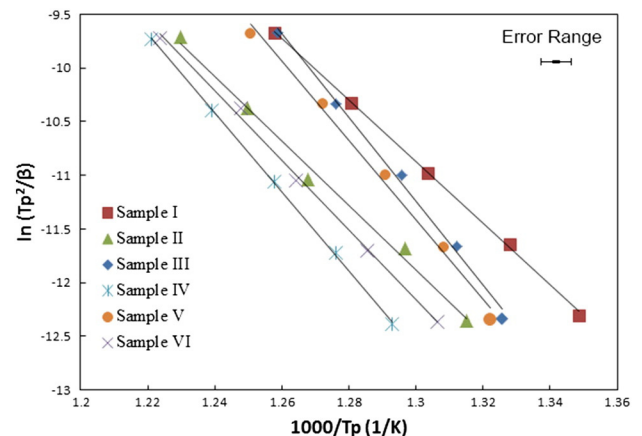
Table 3
Characteristic thermal properties of T_g, T_x, and ΔT_x, at 40 K/min for 3mm diameter as-cast amorphous rods.

Sample	Composition (at.% ± 0.5%)	T_g (K)	T_x (K)	ΔT_x (K)
III	$Zr_{55.5}Ni_{20.6}Al_{14.7}Cu_{6.5}Nb_{2.7}$	722	771	49
V	$Zr_{54.9}Ni_{19.9}Al_{15.0}Cu_{6.3}Nb_{3.9}$	729	776	47

Fig. 6. Kissinger plot for suction cast 3 mm diameter rods of Zr-Ni-Al-Cu-Nb alloys using peak temperature of the first crystallization peak. Error range is shown in the top right corner. (Compositions I–VI as shown in Table 1).

of crystallization behavior for these samples. In addition, linear regression showed each tested sample to have a R^2 greater than 99%.

The activation energy was also calculated using the Ozawa and Cheng equations to compare with the results obtained via Kissinger analysis. The Ozawa equation can be expressed as follows [31]:

$$\ln\beta = \frac{-E_a}{T} + constant \qquad (2)$$

where β is the heating rate, E_a is the activation energy and T is the peak temperature of the first crystallization peak. The activation energy for this equation is obtained through the product of the gas constant and the slope of the linear fitting line when plotting $\ln(\beta)$ versus $1000/T$. While Cheng's equation is stated as [32]:

$$\ln\frac{T_f^2}{\beta} = \frac{E_a}{RT_f} + \ln\frac{E_a}{R} - \ln\nu \qquad (3)$$

where T_f is the inflection point of the first crystallization peak, β the heating rate, E_a the activation energy, ν the frequency factor, and R the gas constant. The same approach as Kissinger is used to determine the activation energy with the only difference being the use of T_f instead of T_p as previously shown in Eq. (1). Fig. 7 shows differential DSC (DDSC) curves which were constructed in order to determine T_f for each sample. While Cheng's equation was originally meant for oxide glasses and not metallic glasses, Wang et al. [33] demonstrated its effectiveness for calculating activation energies for a $Zr_{70}Cu_{20}Ni_{10}$ bulk metallic glass.

Fig. 8 shows a comparison between the activation energies calculated through Kissinger, Ozawa and Cheng's equations. It can be seen that Kissinger and Ozawa follow a similar trend, with activation energies calculated through Ozawa's equation being consistently higher, as noted in similar alloys [32,33]. The activation energies calculated through Cheng's equation for amorphous samples (III and V) gave equal or lower values than Kissinger and Ozawa, which is consistent with Wang's observations in the $Zr_{70}Cu_{20}Ni_{10}$ alloy [33]. Activation energy values calculated for samples with pre-existing crystals using Cheng's equation were inconsistent with the values calculated through the other methods. Even though Cheng's equation gives lower values for amorphous samples, it is unable to capture the effects of pre-existing crystalline phases on thermal stability. As seen in XRD and SEM, Sample IV shows crystallization is present; however, Cheng's equation calculates this sample as having a higher activation energy than the amorphous samples (III and V). This fault in Cheng's equation suggests that Kissinger and Ozawa analyses are more appropriate models for calculating activation energy for BMGs. Sticking with Kissinger analysis, the calculated E_a values for samples I–VI are given in Table 4. It is also noted that the activation energy calculated for samples III and V through Kissinger are greater than the
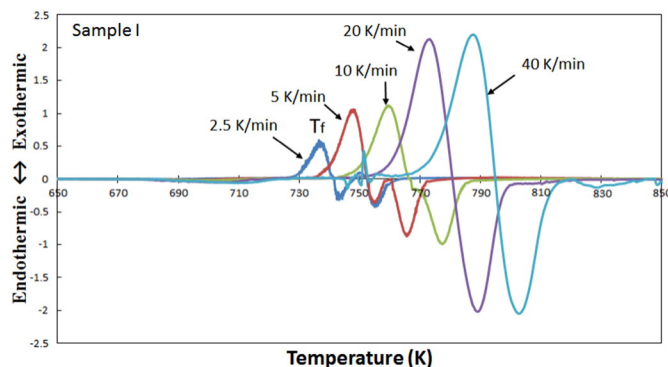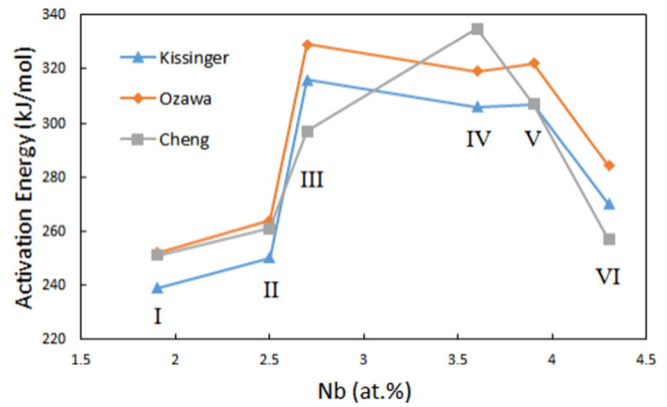

Fig. 8. Comparison of activation energy found through Kissinger, Ozawa and Cheng analysis with increasing Nb content (Compositions I–VI given in Table 1).

$(Zr_{0.645}Ni_{15.5}Al_{11.5}Cu_{8.5})_{100\ -\ x}Nb_x$ alloys by Iqbal and Akhter, and comparable to the $Zr_{60}Cu_{20}Al_{10}Ni_{10}$ alloy by Zhuang et al. [34,35]. These results suggest that Samples III and V are more thermodynamically stable and possess a higher GFA.

Comparing thermal properties for the amorphous alloys (III and V) suggests that Sample III has a higher GFA due to the slightly higher values in both ΔT_x and E_a [3,4,27]. This alloy contained a Nb concentration of 2.7 at.%, and is consistent with similar alloys [9,12]. This finding demonstrates there is a possibility that the critical diameter of the new alloy casted by Li and his colleagues [21] could be even further increased if cast at 2.7 at.% Nb. Further work is required to find the optimal concentration within the high GFA region. It is also noted that the activation energy for the initial crystallization peak is higher for amorphous samples (III and V) compared to crystalline samples (I, II and VI). The higher activation energy indicates that the amorphous structures are more stable as they would require more energy to crystallize. The increased energy requirement is most likely associated with a lack of heterogeneous nucleation sites present in the amorphous samples. Crystalline samples contain pre-existing crystals that serve as effective nucleation sites (as seen in Fig. 2). Crystallization of amorphous samples is a multi-step reaction as indicated by the multiple crystallization peaks in DSC seen in Fig. 3. The lack of nucleation sites dictate that c-Zr_2Ni crystals will form in the initial step before fully crystallizing.

4. Conclusions

In this paper, we conducted a comprehensive investigation of the influence of niobium and oxygen on crystallization behavior and glass forming ability in $(Zr_{56}Ni_{20}Al_{15}Cu_5)_{100\ -\ x}Nb_x$ (from x = 1.9 to 4.3 at.%) alloys. In order to investigate their role, XRD, SEM imaging

Fig. 7. Example of the DDSC curves for Sample I used to find T_f.

Table 4
Peak temperature (T_p) at 10 K/min and activation energies (E_a) of the first crystallization peak measured through Kissinger Analysis for 3 mm diameter as-cast rods and comparison to literature.

Sample	Composition (at.% $\pm$ 0.5%)	T_p (K)	E_a (kJ/mol)
I	$Zr_{58.8}Ni_{20.0}Al_{14.5}Cu_{4.8}Nb_{1.9}$	767	239
II	$Zr_{55.4}Ni_{21.3}Al_{15.4}Cu_{5.4}Nb_{2.5}$	789	250
III	$Zr_{55.5}Ni_{20.6}Al_{14.7}Cu_{6.5}Nb_{2.7}$	772	316
IV	$Zr_{55.0}Ni_{20.3}Al_{15.9}Cu_{5.3}Nb_{3.6}$	795	306
V	$Zr_{54.9}Ni_{19.9}Al_{15.0}Cu_{6.3}Nb_{3.9}$	775	307
VI	$Zr_{54.5}Ni_{20.7}Al_{15.2}Cu_{5.2}Nb_{4.3}$	791	270
[34]	$Zr_{0.645}Ni_{15.5}Al_{11.5}Cu_{8.5}$	–	260
[34]	$(Zr_{0.645}Ni_{15.5}Al_{11.5}Cu_{8.5})_{98}Nb_2$	–	232
[35]	$Zr_{60}Cu_{20}Al_{10}Ni_{10}$	–	326

and DSC were conducted and the resulting data was analyzed. The following conclusions can be drawn:

1. A high glass forming range was produced between 2 and 4 at.% Nb. Alloys with Nb concentration above and below this range was found to have formed $Zr_3NiO_{1.17}$ and $CuZr_2$ crystals upon casting, as seen in XRD spectra.
2. Increased solute oxygen content can destabilize the supercooled liquid region and form crystals during casting even within high glass forming ranges. Having pre-existing oxide present also showed signs of crystal nucleation, but was much less detrimental on the GFA. Therefore, not only does the amount of oxygen present play a key role on the GFA, but also the state in which it exists within BMG alloys.
3. Deconvoluting the multiple peaks seen in DSC curves for amorphous samples revealed the relationship between each phase transition with increasing heating rates. Pairing with XRD allowed for identification of each peak and demonstrated the importance of forming the c-Zr_2Ni phase. This phase was seen to follow two separate crystallization pathways into either t-Zr_2Ni or Zr_5Ni_4Al.
4. Kissinger, Ozawa and Cheng methods were used to calculate the activation energy for samples with pre-existing crystals and amorphous samples. Kissinger and Ozawa showed similar trends, with Ozawa consistently calculating higher values of activation energy. Cheng's method gave the lowest values of activation energy for amorphous samples, but was inconsistent when applying to samples with pre-existing crystals.
5. Thermal analysis for amorphous samples (III and V) suggest that sample III could have a higher GFA as a result of slightly increased values in ΔT_x (49 K versus 47 K) and activation energy (316 kJ/mol versus 307 kJ/mol by Kissinger) and potentially result in an increased critical casting diameter.

Acknowledgements

References

[1] A. Inoue, Stabilization of metallic supercooled liquid and bulk amorphous alloys, Acta Mater. 48 (2000) 279–306.
[2] W.L. Johnson, Bulk glass-forming metallic alloys: science and technology, MRS Bull. 24 (10) (1999) 42–56.
[3] J.F. Loffler, Review: bulk metallic glasses, Intermetallics 11 (2003) 529–540.
[4] W.H. Wang, C. Dong, C.H. Shek, Bulk metallic glasses, Mater. Sci. Eng. R 44 (2004) 45–89.
[5] Z.P. Lu, C.T. Liu, A new glass-forming ability criterion for bulk metallic glasses, Acta Mater. 50 (2002) 3501–3512.
[6] W.H. Wang, Roles of minor additions in formation and properties of bulk metallic glasses, Prog. Mater. Sci. 52 (2007) 540–596.
[7] J. Cui, J.S. Li, J. Wang, H.C. Kou, J.C. Qiao, S. Gravier, J.J. Blandin, Crystallization kinetics of Cu38Zr46Ag8Al8 bulk metallic glass in different heating conditions, J. Non-Cryst. Solids 404 (2014) 7–12.
[8] Q.K. Jiang, X.P. Nie, Y.G. Li, Y. Jin, Z.Y. Chang, X.M. Huang, J.Z. Jiang, Ni-free Zr-based bulk metallic glasses with critical diameter above 20 mm, J. Alloys Compd. 443 (2007) 191–194.
[9] A. Inoue, T. Shibata, T. Zhang, Effect of additional elements on glass transition behavior and glass formation tendency of Zr-Al-Cu-Ni alloys, Mater. Trans. JIM 36 (12) (1995) 1420–1426.
[10] C. Suryanarayana, A. Inoue, Thermal Stability of Metallic Glasses, Bulk Metallic Glasses, FL, CRC Press Taylor & Francis Group, Boca Raton 2011, pp. 208–211.
[11] Y.F. Sun, C.H. Shek, B.C. Wei, W.H. Li, Y.R. Wang, Effect of Nb content on the microstructure and mechanical properties of Zr-Cu-Ni-Al-Nb glass forming alloys, J. Alloys Compd. 403 (2005) 239–244.
[12] W. Dong, H. Zhang, W. Sun, B. Ding, Z. Hu, Formation, thermal stability and mechanical properties of Zr-Nb-Cu-Ni-Al bulk metallic glasses, Mater. Trans. 47 (5) (2006) 1294–1298.
[13] C. Suryanarayana, A. Inoue, Computational Approaches, Bulk Metallic Glasses, FL, CRC Press, Boca Raton 2011, pp. 126–128.
[14] F. Szuecs, C.P. Kim, W.L. Johnson, Mechanical properties of Zr56·2Ti13.8Nb5·0Cu6.9Ni5·6Be12.5, Acta Mater. 53 (2001) 1507–1513.
[15] G.Y. Sun, G. Chen, G.L. Chen, Comparison of microstructures and properties of Zr-based bulk metallic glas composites with dendritic and pherical bcc phase precipitates, Intermetallics 15 (2007) 632–634.
[16] M.L. Lee, Y. Li, C.A. Schuh, Effect of a controlled volume fraction of dendritic phases on tensile and compressive ductility in La-based metallic glass matrix composites, Acta Mater. 52 (2004) 4121–4131.
[17] Z. Bian, H. Kato, C.L. Qin, W. Zhang, A. Inoue, Cu-Hf-Ti-Ag-Ta bulk metallic glass composites and their properties, Acta Mater. 53 (2005) 2037–2048.
[18] A. Gebert, J. Eckert, L. Schultz, Effect of oxygen on phase formation and thermal stability of slowly cooled Zr65Al7·5Cu17.5Ni10 metallic glass, Acta Mater. 46 (15) (1998) 5475–5482.
[19] J. Eckert, N. Mattern, M. Zinkevitch, M. Seidel, Crystallization behavior and phase formation in Zr-Al-Cu-Ni metallic glass containing oxygen, Mater. Trans. JIM 39 (6) (1998) 623–632.
[20] B.S. Murty, D.H. Ping, K. Hono, A. Inoue, Influence of oxygen on the crystallization behavior of Zr65Cu27·5Al7.5 and Zr66·7Cu33.3 metallic glasses, Acta Mater. 48 (2000) 3985–3996.
[21] Y. Li, W. Zhang, F. Qin, A. Makino, Mechanical properties and corrosion resistance of a new Zr56Ni20Al15Nb4Cu5 bulk metallic glass with a diameter up to 25 mm, J. Alloys Compd. 615 (2014) 571–574.
[22] H. Choi-Yim, R.D. Conner, F. Szuecs, W.L. Johnson, Processing, microstructure and properties of ductile metal particulate reinforced Zr57Nb5Al10Cu15·4Ni12.6 bulk metallic glass composites, Acta Mater. 50 (2002) 2737–2745.
[23] M. Naka, K. Hashimoto, T. Masumoto, Corrosion behavior of amorphous crystalline Cu50Ti50 and Cu50Zr50 alloys, J. Non-Cryst. Solids 30 (1) (1978) 29–36.
[24] C.L. Qin, W. Zhang, K. Asami, H. Kimura, X.M. Wang, A. Inoue, A novel Cu-based BMG composite with high corrosion resistance and excellent mechanical properties, Acta Mater. 54 (14) (2006) 3713–3719.
[25] ASTM International, ASTM E1409: Standard Test Method for Determination of Oxygen and Nitrogen in Titanium and Titanium Alloys by Inert Gas Fusion, 2013.
[26] J. Igel, D.W. Kirk, C.V. Singh, S.J. Thorpe, A practical investigation of the production of Zr-Cu-Al-Ni bulk metallic glasses by arc melting and suction casting, Mater. Trans. 56 (11) (2015) 1834–1841.
[27] Y.-h. Li, W. Zhang, C. Dong, J.-b. Qiang, A. Makino, Correlation between the glass-forming ability and activation energy of crystallization for Zr75 − xNi25Alx metallic glasses, Int. J. Miner. Metall. Mater. 20 (5) (2013) 445–449.
[28] L. Lin, W. Zhi-Fang, C. Li, A kinetic study of the non-isothermal crystallization of a Zr-based bulk metallic glass, Chin. Phys. Lett. 19 (10) (2002) 1483–1486.
[29] J. Pang, Y. Wang, M.J. Tan, K.M. Liew, Thermal properties of metallic glasses: heating rate dependence and their correlation, Mater. Lett. 126 (2014) 81–84.
[30] H.E. Kissinger, Reaction kinetics in differential thermal analysis, Anal. Chem. 29 (11) (1957) 1702–1706.
[31] T. Ozawa, Kinetic analysis of derivative curves in thermal analysis, J. Therm. Anal. 2 (1970) 301–324.
[32] K. Cheng, Evaluation of crystallization kinetics of glasses by non-isothermal analysis, J. Mater. Sci. 36 (2001) 1043–1048.
[33] H.-R. Wang, Y.-L. Gao, Y.-F. Ye, G.-H. Min, Y. Chen, X.-Y. Teng, Crystallization kinetics of an amorphous Zr-Cu-Ni alloy: calculation of the activation energy, J. Alloys Compd. 353 (2003) 200–206.
[34] M. Iqbal, J.I. Akhter, Influence of Y and Nb addition on crystallization behavior and mechanical properties of Zr-Ni-Al-Cu-M bulk amorphous alloys, Adv. Mater. Res. 326 (2011) 11–18.
[35] Y.X. Zhuang, T.F. Duan, H.Y. Shi, Calorimetric study of non-isothermal crystallization kinetics of Zr60Cu20Al10Ni10 bulk metallic glass, J. Alloys Compd. 509 (2011) 9019–9025.